TUNING PROCEDURE FOR THE RESILIENT SLIP-FRICTION JOINT (RSFJ)

Nicholas Chan¹, Ashkan Hashemi² and Pierre Quenneville³

(Submitted April 2024; Reviewed July 2024; Accepted May 2025)

ABSTRACT

Self-centering friction dampers like the Resilient Slip-Friction Joint (RSFJ) are increasingly relevant for their ability to (1) damp earthquake-induced vibrations without degradation, and (2) prevent residual deformations after earthquakes, thus reducing both damage and downtime. One of their main advantages is a highly customizable load-deformation behaviour, which makes them versatile across various structural applications. Taking advantage of this, however, requires a degree of intuition and iteration to obtain suitable designs. This paper derives an objective and systematic procedure to generate all possible combinations of damper parameters that can produce a custom flag-shaped hysteresis. Equations are obtained to calculate the parameters explicitly and the procedure is validated with existing experimental data. A modelling example is included to demonstrate how the dampers in a three-storey structure can be tuned automatically to provide the global response required. Nonlinear time-history analyses show that the procedure is effective at tuning the dampers simultaneously to achieve the displacement targets and linear deformation profile specified from a displacement-based design.

https://doi.org/10.5459/bnzsee.1691

INTRODUCTION

Resilient Slip-Friction Joint (RSFJ)

Widespread damage and downtime in recent earthquakes have revealed a wider societal desire for improved levels of seismic performance [1,2]. This is reflected in a surge of research on self-centering systems in the last ten years as such systems could expedite post-earthquake re-occupancy and recovery of functions [3]. These systems include self-centering friction dampers which provide damping and self-centering in a compact unit. The repeatability of damping via friction makes it possible to conduct non-destructive testing prior to installation, thus increasing its reliability in actual earthquakes.

One such damper is the Resilient Slip Friction Joint (RSFJ) which was invented in New Zealand after the Christchurch earthquakes [4]. As Figure 1 shows, grooves are profiled into middle plates and cap plates, which meet and slide along the inclined slopes. These are clamped together by pre-compressed disc springs to induce re-centering after earthquakes.

The tapers in the RSFJ induce a wedging action whereby axial deformation causes an associated transverse motion. The transverse expansion leads to a proportional increase in the spring/friction forces. This allows greater hysteretic areas delineated by the two slopes k_L and k_H in Figure 2.

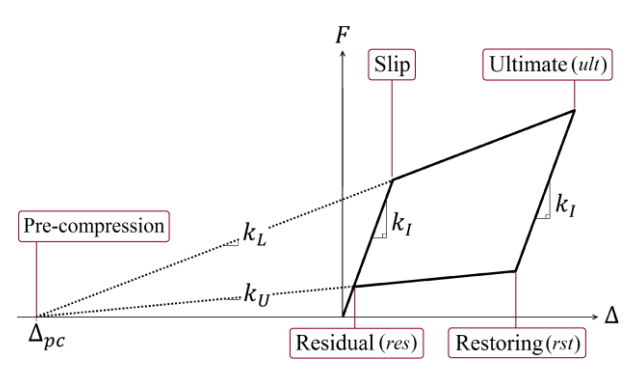


Figure 2: Typical flag-shaped hysteresis.

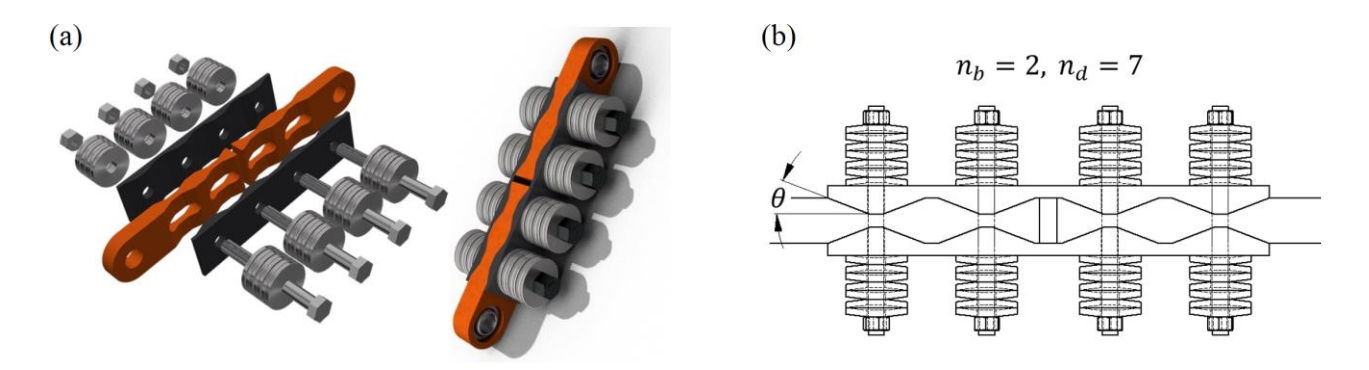


Figure 1: Illustrating the RSFJ (a) 3D view, (b) Cross-section.

¹ Corresponding Author, Research Assistant, The University of Auckland, Auckland. <u>jcha367@aucklanduni.ac</u>

² Senior Lecturer, The University of Auckland, Auckland. <u>a.hashemi@auckland.ac.nz</u> (Member)

³ Professor, The University of Auckland, Auckland. <u>p.quenneville@auckland.ac.nz</u> (Member)

The additional damping helps absorb substantial kinetic energy, and approaches that of ratcheting dampers [5,6]. Experimental studies on the RSFJ have demonstrated its versatility in different seismic-resisting systems [7]. Other researchers are also investigating similar variants with generic names like variable friction dampers [8,9].

The geometric relationship between the RSFJ axial deformation $(\Delta_{ult} - \Delta_{slip})$ and the deformation of the stack of disc springs is shown in Equations 1 and 2. The variables shown here are the number of disc-springs per splice and per side n_d , bolt/disc-spring force when pre-stressed at the slip point F_{bpr} and when loaded at the ultimate point F_{bu} , the deformation of each disc spring between slip and ultimate points d_s , the stiffness of a disc spring k_d and the groove angle θ .

$$\Delta_{ult} - \Delta_{slip} = \frac{2n_d d_s}{\tan \theta} \tag{1}$$

$$d_s = \frac{F_{bu} - F_{bpr}}{k_d} \tag{2}$$

The forces at slip F_{slip} , ultimate F_{ult} , restoring F_{rst} , and residual F_{res} stages are expressed in Equations 3 to 6. In addition to the variables described earlier, n_b denotes the number of bolts per splice, and μ denotes the coefficient of friction.

$$F_{slip} = 2n_b F_{bpr} \frac{\tan \theta + \mu}{1 - \mu \tan \theta}$$
 (3)

$$F_{ult} = 2n_b F_{bu} \frac{\tan \theta + \mu}{1 - \mu \tan \theta} \tag{4}$$

$$F_{rst} = 2n_b F_{bu} \frac{\tan \theta - \mu}{1 + \mu \tan \theta}$$
 (5)

$$F_{res} = 2n_b F_{bpr} \frac{\tan \theta - \mu}{1 + \mu \tan \theta} \tag{6}$$

Motivation for an Alternate Tuning Procedure

While the damper can be tuned to achieve a range of flagshaped hysteresis, the process is not entirely straightforward. Obtaining the right combination of design parameters requires some intuition and iteration because the parameters can have multiple and overlapping effects on the resulting flag-shape.

Also, not all possible combinations may have been considered even with some prior experience. Hence, this paper presents a systematic procedure to generate damper configurations that can produce a specified flag-shaped hysteresis for applications like displacement-based design. Some of the benefits of the proposed procedure are:

- The proposed procedure allows a straightforward method to quantify the damper properties explicitly and avoids the need for manual trial-and-error. Thus, designers with different levels of familiarity can estimate damper parameters easily (e.g., for cost and size estimates), thus supporting technology transfer into engineering practice.
- As the procedure is fully automated, it lends itself well to research purposes and can reduce the substantial amount of labour needed to set up numerical models for parametric studies. Examples include designing numerous models to characterise seismic performance and generating models to feed machine learning algorithms and develop prediction tools

This paper begins by seeking an explicit method from first principles to quantify the damper parameters based on an input performance required. The method is then applied and compared against existing experimental data. This is followed by a design and modelling example of a structure equipped with tension-only braces.

In this example, an algorithm is coded and implemented to determine the flag-shapes required automatically. From the flag-shapes, suitable RSFJ configurations can be generated using the explicit method. Hence, the two-stage procedure aims to tune the devices systematically and simultaneously to achieve a specified structural performance. Finally, the design solution is verified through nonlinear time-history analyses of the structure.

The proposed procedure does not clash with established design techniques like force- or displacement-based design methodologies. Instead, it is intended to complement these methodologies by improving the relevant steps of the (design and modelling) processes for structures containing the RSFJ. This is shown in Fig. 3 for a displacement-based design process, which may benefit from reduced iterations.

Therefore, the goal is to develop an alternate procedure to design and tune the RSFJ more efficiently and objectively. Unlike standard frames with yielding members, the entire flagshape desired for the structure can be matched closely through this procedure. This includes the amount of dissipation desired by the designer.

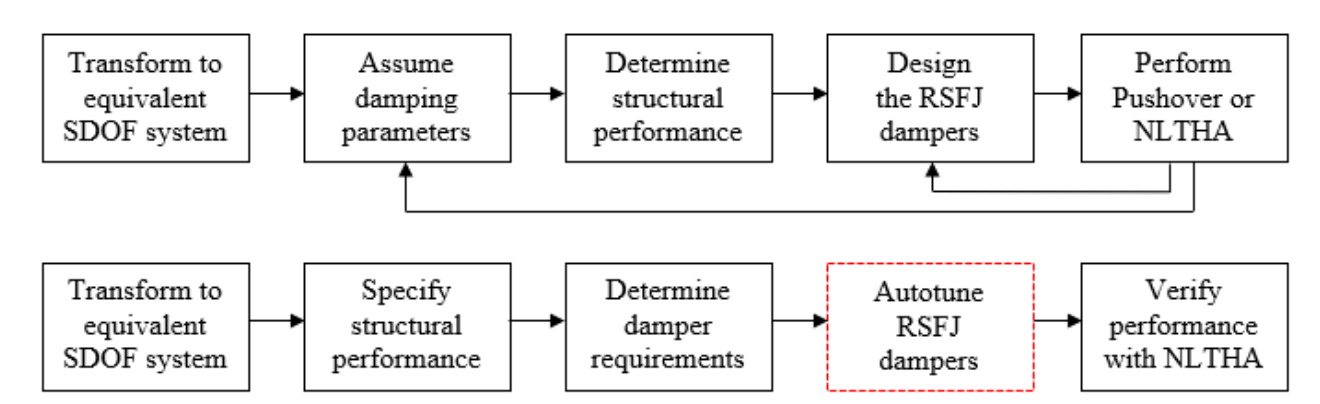


Figure 3: Displacement-based design method with the RSFJ. Typical process (top). Proposed procedure (bottom).

METHODOLOGY

The proposed procedure aims to generate damper configurations that result in a structural response sought by the designer. The procedure is composed of two stages. The first stage involves pushover analyses in a structural model to find out what damper behaviours are needed to achieve the global structural response specified by the user. This stage is presented in a later section via a numerical modelling example.

The second stage involves calculations to determine what are the damper properties that will provide the damper behaviours determined from the first stage of the procedure. This section derives an explicit method to generate RSFJ configurations for the second stage.

The method directly calculates four main parameters of the RSFJ that largely control its behaviour: number of bolts per splice n_b , number of disc springs per splice and per side n_d , groove angle θ , and pre-stressing force on the bolt/disc-spring F_{bpr} . The inputs required are the flag-shape values, friction coefficient μ , disc-spring stiffness k_d and bolt/disc-spring ultimate force F_{bu} which is the maximum load intended on the bolt/disc-spring.

The first step is to solve for the taper angle θ . The solution for θ is derived from Equations 4 and 5, which results in Equations 7–10 after some algebraic manipulation. These equations relate the angle θ directly to a dissipation parameter r, which is itself expressed in terms of the coefficient of friction μ , and the difference in forces between loading F_{ult} and unloading F_{rst} stages.

$$\frac{F_{ult}}{F_{rst}} = \left(\frac{\tan\theta + \mu}{\tan\theta - \mu}\right) \left(\frac{1 + \mu \tan\theta}{1 - \mu \tan\theta}\right) \tag{7}$$

$$0 = \tan^2 \theta - \left(\frac{\mu^2 + 1}{\mu}\right) \left(\frac{F_{ult} - F_{rst}}{F_{ult} + F_{rst}}\right) \tan \theta \tag{8}$$

$$\theta = \operatorname{atan}\left(r - \sqrt{r^2 - 1}\right) \tag{9}$$

$$r = \frac{\mu^2 + 1}{2\mu} \left(\frac{F_{ult} - F_{rst}}{F_{ult} + F_{rst}} \right) \tag{10}$$

Note that for Equation 9 to have a valid solution, r must be greater than 1. Using this fact in Equation 10 and rearranging into Equation 11, it means that the restoring force F_{rst} is bounded by the lower and upper limits given by Equations 12 and 13. Intuitively, the flag-shape is thinnest at $\theta=45^\circ$ and thickest at $\theta=\tan(\mu)$, as smaller wedging angles result in larger normal (friction) forces and thus a thicker flag-shape. In cases where a specific groove angle θ is pre-determined, e.g. with damper manufacturers, then the first step of calculating θ is not needed because the dissipation is already fixed and the number of unknowns reduced.

$$\frac{F_{ult} - F_{rst}}{F_{ult} + F_{rst}} \ge \frac{2\mu}{\mu^2 + 1} \tag{11}$$

$$F_{rst} > 0 (12)$$

$$F_{rst} < F_{ult} \left(\frac{1-\mu}{1+\mu}\right)^2 \tag{13}$$

From Equations 3 and 4, the pre-compression force in the bolts and disc springs is related by Equation 14:

$$F_{bpr} = \left(\frac{F_{slip}}{F_{ult}}\right) F_{bu} \tag{14}$$

Next, the number of bolts is obtained in Equation 15 by rearranging Equation 4:

$$n_b = \frac{F_{ult}}{2F_{bu}} \left(\frac{1 - \mu \tan \theta}{\mu + \tan \theta} \right)$$
 (15)

And the number of discs via Equation 16 from substituting Equation 2 into Equation 1:

$$n_d = \left(\frac{\Delta_{ult} - \Delta_{slip}}{F_{bu} - F_{bpr}}\right) \left(\frac{k_d \tan \theta}{2}\right) \tag{16}$$

Thus, the four parameters calculated (n_b, n_d, θ) and F_{bpr}) represent a solution for the exact flag-shape required. However, the number of bolts and disc springs are decimal values, which are not possible in practice. Hence, integer values must be chosen for n_b and n_d . This reduces the number of solution variables to 2 terms: parameters θ and F_{bpr} . It means that two constraints must be relaxed. One recourse is to relax the dissipation requirement (k_U) since the dynamic response is less sensitive to the dissipation when compared to the backbone curve [10,11]. In addition, relaxing the ultimate deformation constraint allows the backbone to be preserved and prioritized. So, once the choices are made for n_b and n_d (discussed subsequently), parameters θ and F_{bpr} may then be revised as follows

Using Equations 1–4, the loading stiffness can also be expressed as Equations 17 and 18:

$$k_L = \frac{F_{ult} - F_{slip}}{\Delta_{ult} - \Delta_{slip}} \tag{17}$$

$$k_L = k_d \left(\frac{n_b}{n_d}\right) \left(\frac{\tan \theta + \mu}{1/\tan \theta - \mu}\right) \tag{18}$$

Rearranging Equation 18 into Equations 19–22 gives an expression for the new taper angle θ :

$$0 = \tan^2 \theta + \tan \theta \left(1 + \frac{k_L}{k_d} \frac{n_d}{n_b} \right) (\mu) - \frac{k_L}{k_d} \frac{n_d}{n_b}$$
 (19)

$$\theta = \tan\left(\sqrt{x + y^2} - y\right) \tag{20}$$

where the terms x and y are calculated by substituting the integer values chosen for n_b and n_d :

$$x = \frac{k_L}{k_d} \frac{n_d}{n_b} \tag{21}$$

$$y = \frac{\mu}{2}(x+1)$$
 (22)

Finally, the pre-compression force is revised by rearranging Equation 3 into Equation 23:

$$F_{bpr} = \frac{F_{slip}}{2n_b} \left(\frac{1 - \mu \tan \theta}{\mu + \tan \theta} \right)$$
 (23)

A final check requires that $\theta \ge \operatorname{atan}(\mu)$ to allow re-centering.

Choosing n_b and n_d is an important stage involving a trade-off between matching the deformation capacity $(\Delta_{ult} - \Delta_{slip})$ versus matching the dissipation capacity (F_{ult}/F_{rst}) .

To produce the exact dissipation required, Equation 7 shows that the angle θ must be the same for both decimal and integer sets of values. This means that the ratio n_b/n_d in Equation 18 must also be the same for both sets to maintain the same backbone (k_L) as before. Thus, if the ratios n_b/n_d are similar before and after adjustment (i.e., n_b and n_d both increase or decrease), then the dissipation will match very well but the deformation may not.

On the other hand, to produce the exact deformation required, Equation 1 must be constant. Substituting in Equation 2 indicates that the ratio $n_d/\tan\theta$ must be the same for both decimal and integer sets of values. However, if n_d decreases in Equation 16, $\tan\theta$ decreases in Equation 15 and causes n_b to increase to maintain the same ultimate force and deformation (backbone). Thus, maintaining the ratio $n_d/\tan\theta$ requires an inverse relationship between n_b and n_d (i.e., n_b increase/decrease while n_d decrease/increase). In this case, the deformation will match very well but the dissipation may not.

To determine the best combination of parameters, a range of options can be generated and ranked according to the weighted error ϵ_W in Equation 24. It applies weights w_F and w_Δ to the errors in forces/dissipation ϵ_F and deformation ϵ_Δ capacities. The superscript t (as in F^t_{ult} , F^t_{rst} , Δ^t_{ult} and Δ^t_{slip}) denotes the target (required) forces and deformations. Possible weights are $w_F = 0.5$ and $w_\Delta = 1.0$.

$$\epsilon_w = \epsilon_F + \epsilon_\Delta \tag{24}$$

where the weighted error terms are:

$$\epsilon_F = w_F \left| 1 - \left(\frac{F_{ult} - F_{rst}}{F_{ult}^t - F_{rst}^t} \right) \right|$$

$$\epsilon_{\Delta} = w_{\Delta} \left| 1 - \left(\frac{\Delta_{ult} - \Delta_{slip}}{\Delta_{ult}^t - \Delta_{slip}^t} \right) \right|$$

The options can be filtered based on minimum deformation or dissipation requirements. For instance, possible filter criteria that can be used are:

- 1. Joint deformation must be above 95% of the required deformation, i.e. $(\Delta_{ult} \Delta_{slip})/(\Delta_{ult}^t \Delta_{slip}^t) \ge 0.95$.
- 2. Joint dissipation must be above 85% of the required dissipation, i.e. $(F_{ult} F_{rst})/(F_{ult}^t F_{rst}^t) \ge 0.85$.

EXPERIMENTAL VALIDATION

The tuning procedure is validated experimentally using test results from Bagheri et al. (2020) [12], as complete data are available from testing both the disc spring component and the overall behaviour of the joint (Figure 4). Thus, the procedure is applied with the given properties of the disc spring to produce the design options for the RSFJ.



Figure 4: RSFJ tested by Bagheri et al. (2020) [12].

Looking at the test data in Figure 5, the flag-shape begins slipping at 90 kN and reaches approximately 225 kN at about 30 mm of deformation, before unloading to a residual force of 30 kN as the joint re-centers. Plugging these values into the procedure, with an assumed coefficient of friction of 0.15, several options of the RSFJ are generated and listed in Table 1 in no specific order.

Table 1: RSFJ options (#1 - #7) generated by the procedure.

#	n_b	n_d	θ	F _{bpr}	F _{bu}	ϵ_F	ϵ_{Δ}	ϵ_w
1	2	4	14.6	52.7	132	0.072	0.004	0.076
2	2	5	16.7	47.7	132	0.005	0.179	0.184
3	2	6	18.6	43.9	132	0.055	0.338	0.394
4	3	3	9.8	45.3	132	0.203	0.278	0.481
5	3	4	11.8	40.4	132	0.109	0.509	0.618
6	3	5	13.6	36.9	132	0.026	0.716	0.742
7	3	6	15.1	34.2	132	0.048	0.905	0.953

The coefficient of friction greatly influences the predicted forces and will depend on the specific material and surface conditions (e.g., lubrication). From past studies, values of the friction coefficient range between 0.15 [4,13] and 0.19 [14] with the variation also attributed to the differences in loading speed. These values have provided accurate predictions of the cyclic behaviour observed from tests. Hence, the value of 0.15 is assumed for the friction coefficient.

Figure 5 compares the test data against the RSFJ design options generated by the procedure automatically. Options 1 and 2 appear to be close to the original flag-shape intended. Specifically, Option 2 provides the closest dissipation and results in the same joint parameters selected by the authors for testing in Fig. 5, which are $n_b = 2$, $n_d = 5$, and $\theta = 17^\circ$.

However, the procedure also reveals other possible options available to the designer as Table 1 shows. All these can provide the same backbone required but with different amounts of deformation and dissipation prior to activation of the secondary fuse (softening) which is beyond the scope of this paper. Thus, the different options generated by the procedure can have identical slopes on their backbones, but it requires the displacement capacities to be unrestrained and allowed to differ between the options.

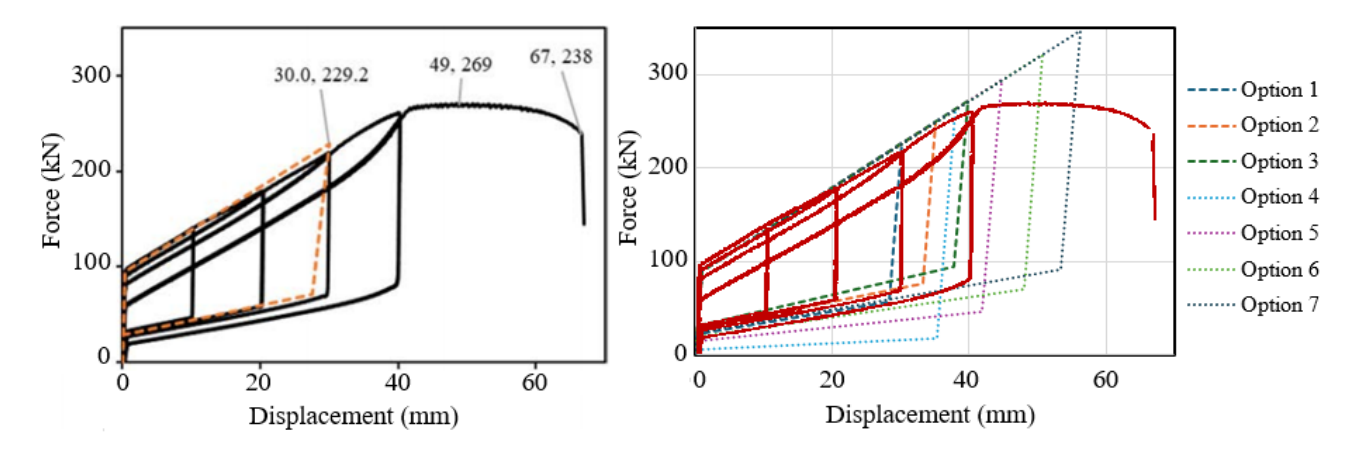


Figure 5: Test data from Bagheri et al. (2020) [12] and flag-shapes of the RSFJ options generated.

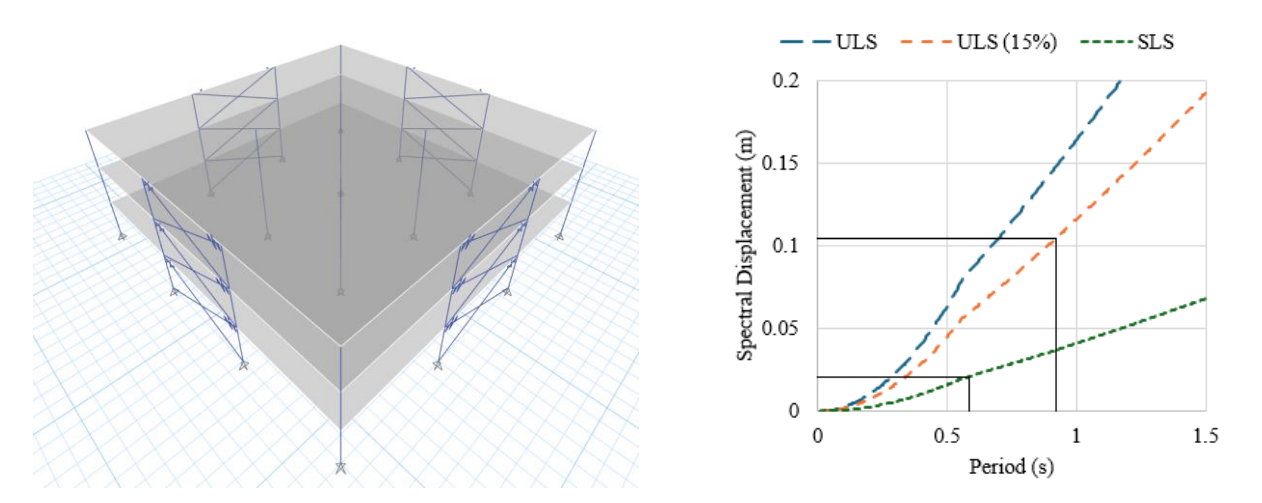


Figure 6: (a) Modelled structure with tension-only braces, and (b) Displacement spectra used for the DDBD.

DESIGN EXAMPLE

The dampers can be modelled in structural analysis software like ETABS and tuned automatically to achieve the structural response desired by the user. As Figure 6 shows, they are applied in tension-only braces of a low-rise building designed for Wellington, New Zealand. The overall dimensions are 24 x 24 x 9 m, and each floor supports a seismic mass of 355 ton (dead load: 182 ton/floor, live load: 173 ton/floor).

The direct displacement-based design (DDBD) method [15] was used to design the cyclic behaviour of the structure. The target drifts are 0.3% at slip to meet serviceability requirements and 1.5% at the ultimate limit state to reduce the extent of damage to non-structural elements [16]. Figure 6 shows the design spectrum obtained with site hazard factor of 0.4, soil class C, and return period of 500 years (ULS) and 25 years (SLS).

The damped spectrum is calculated using the displacement reduction factor R_{eq} from Eurocode 8 [17] and shown in Equation 25. It assumes a damping ratio ζ of 15% by selecting the restoring base shear as one-quarter of the ultimate base shear [10]. The effective periods are obtained from Figure 6. The effective mass m_e , height h_e , displacements Δ_e and base shears V_b are calculated via Equations 26–31. Table 2 shows the calculations.

$$R_{eq} = \sqrt{\frac{10}{5 + \zeta}} \tag{25}$$

$$m_e = \frac{\left(\sum_{i=1}^3 m_i \Delta_i\right)^2}{\sum_{i=1}^3 m_i \Delta_i^2} \tag{26}$$

$$H_e = \frac{\sum_{i=1}^{3} m_i \Delta_i h_i}{\sum_{i=1}^{3} m_i \Delta_i}$$
 (27)

$$\Delta_{e \text{ (ULS)}} = \frac{\sum_{i=1}^{3} m_i \Delta_i^2}{\sum_{i=1}^{3} m_i \Delta_i}$$
 (28)

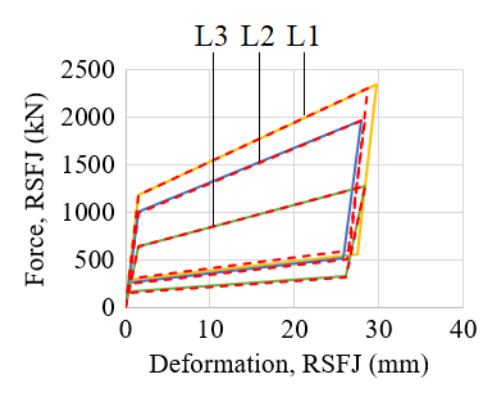
$$\Delta_{e \text{ (SLS)}} = \delta_{SLS} H_e \tag{29}$$

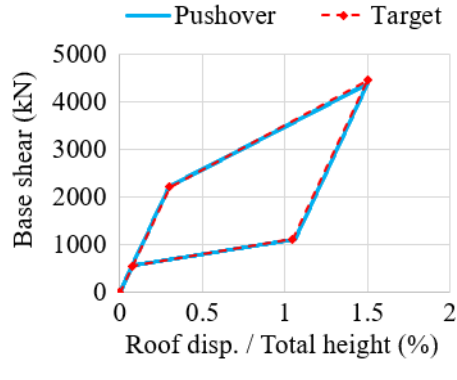
$$V_{b (ULS)} = m_e \left(\frac{2\pi}{T_{e (ULS)}}\right)^2 \Delta_{e (ULS)}$$
(30)

$$V_{b (SLS)} = m_e \left(\frac{2\pi}{T_{e (SLS)}}\right)^2 \Delta_{e (SLS)}$$
(31)

Storey	m	h	Δ	$m\Delta$	$m\Delta^2$	$m\Delta h$		ULS	SLS
	(kg)	(m)	(m)	(kgm)	(kgm²)	(kgm²)			
3	354642	9	0.135	47877	6463	430890	Δ_e	1.5%	0.3%
2	354642	6	0.090	31918	2873	191507	Δ_e	0.105 m	0.021 m
1	354642	3	0.045	15959	718	47877	T_e	0.922 s	0.584 s
	$m_e = 911937 \text{ kg}$	$h_e = 7 \text{ m}$	Σ	95753	10054	670273	V_b	4449 kN	2214 kN

Table 2: Displacement-based design calculations.





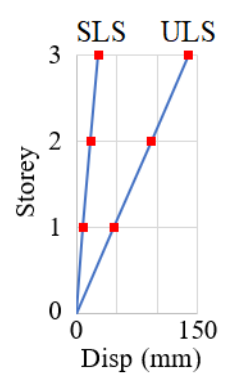


Figure 7: (a) Tuning the dampers to achieve the required, (b) Pushover response, and (c) Deflection profile.

Table 3: Target values for the dampers' flag-shaped hysteresis and corresponding designs generated.

Storey	F_{slip}	F_{ult}	F_{rst}	F_{res}	Δ_{slip}	Δ_{ult}	Δ_{rst}	Δ_{res}	n_b	n_d	$\boldsymbol{ heta}$	F_{bpr}
3	641	1274	321	162	1.5	28.4	26.2	0.4	11	5	15.1	66
2	1000	1976	503	254	1.5	28.4	26.2	0.4	17	5	15.1	67
1	1185	2300	595	305	1.5	28.7	26.5	0.4	21	5	14.4	67

Note: Units in kN, mm. Assume $\mu=0.15$, disc springs linear up to 110 kN at 1.5 mm ($k_d=73.3$ kN/mm) as per Bagheri et al. (2020) [12].

After determining the desired cyclic response of the structure, individual damper elements were tuned to achieve the global response via a series of nonlinear static (pushover) analyses. The following steps outline the tuning procedure used to translate the desired structural response into the dampers' flagshape performance required (i.e., stage 1 from steps 1 to 3.4) and subsequently the corresponding damper configurations (i.e., stage 2 at step 3.5). The numerical model considers the elastic stiffness of the frame implicitly.

- Obtain global responses from the DDBD calculations.
 These are the base shear values at slip, ultimate, and restoring stages, and the inter-story drifts (at each brace) at slip and ultimate stages.
- Specify the load pattern used in the pushover analysis. This
 example uses the equivalent static force distribution as per
 AS/NZS 1170, whereby 8% of the base shear is assigned to
 the top floor and the remaining 92% distributed in
 proportion to each floor's weight and height product.
- Determine the damper configurations needed to achieve these global responses:
- 3.1 With the base shear at slip applied, adjust dampers' k_I until each diagonal registers the target slip drift.
- 3.2 Having found the dampers' slip points, adjust k_L (as nonlinear links) until each braced diagonal registers the target ultimate drift when subjected to the ultimate base shear.
- 3.3 Obtain the dampers' restoring points by unloading the structure to the restoring base shear.

- 3.4 [Optional] Adjust the dampers' initial stiffness to known device values by changing the slip deformation only. The dampers' slip force, ultimate force and ultimate deformation are unchanged. This adjustment may cause the pushover curve to become rounder at the slip point as the dampers' slip progressively, but the ultimate point will be unchanged.
- 3.5 The flag-shape for each damper is now fully defined (Table 3), and the dampers' parameters $(n_b, n_d, \theta, F_{bpr})$ can be calculated through the steps described earlier in the Methodology section. Figure 7 shows the results of the iterations. While the RSFJ can work in both tension and compression, only the tensile behaviour is shown here since the tension-only braces are not subjected to compressive actions.

One question regarding the use of tension-only braces is how far the braces should be tightened, and what does the pretensioning do to the overall system performance. Indeed, this was an important factor during previous tests done by Bagheri et al. (2020) [12], as they observed that the braces were sagging under self-weight if not tightened enough. The sagging was detrimental to the system's performance and lateral resistance, since the braces were sagging and lacking tension. Only after some displacement could the braces extend enough and begin to engage in tension. Hence, the initial slackness led to pinching of the hysteresis loops. To minimize the sagging to an acceptable level, the authors determined that the braces need to be tightened to the force of approximately 5 kN which was achievable by hand.

Table 4: List of ground motions used in the nonlinear time-history analyses.

Event	Year	$\mathbf{M}_{\mathbf{w}}$	R_{JB}	$V_{s,30}$	Record file name in PEER database
Imperial Valley	1940	6.95	6.09	213.44	RSN6_IMPVALL.I_I-ELC270
San Fernando	1971	6.61	58.99	217.92	RSN69_SFERN_TLI249
Imperial Valley	1979	6.53	17.94	196.88	RSN175_IMPVALL.H_H-E12140
Imperial Valley	1979	6.53	4.90	208.91	RSN179_IMPVALL.H_H-E04140
Livermore	1980	5.80	15.84	384.47	RSN215_LIVERMOR_A-SRM340
Coalinga	1983	6.36	30.30	492.43	RSN358_COALINGA.H_H-SC4090
Morgan Hill	1984	6.19	31.34	367.57	RSN453_MORGAN_FRE075
Superstition Hills	1987	6.54	18.48	266.01	RSN722_SUPER.B_B-KRN270
Superstition Hills	1987	6.54	23.85	179.00	RSN729_SUPER.B_B-IVW360
Cape Mendocino	1992	7.01	15.97	457.06	RSN827_CAPEMEND_FOR000
Cape Mendocino	1992	7.01	15.97	457.06	RSN827_CAPEMEND_FOR090
Landers	1992	7.28	161.56	285.28	RSN871_LANDERS_GR2180
Big Bear	1992	6.46	121.75	452.15	RSN913_BIGBEAR_TEM090
Big Bear	1992	6.46	121.75	452.15	RSN913_BIGBEAR_TEM180
Big Bear	1992	6.46	107.18	339.60	RSN918_BIGBEAR_NBI360
Northridge	1994	6.69	27.82	304.68	RSN1000_NORTHR_PIC090
Northridge	1994	6.69	0.00	628.99	RSN1013_NORTHR_LDM334
Northridge	1994	6.69	51.88	268.65	RSN1025_NORTHR_LAN360
Kobe	1995	6.90	0.00	312.00	RSN1119_KOBE_TAZ000
Chi-Chi	1999	7.62	42.15	169.84	RSN1228_CHICHI_CHY076-E
Hector Mine	1999	7.13	77.01	376.91	RSN1773_HECTOR_CAB270
Hector Mine	1999	7.13	179.29	349.43	RSN1799_HECTOR_OBR090
Chi-Chi	1999	6.20	102.36	228.84	RSN2987_CHICHI.05_CHY099N
Chi-Chi	1999	6.30	30.44	487.27	RSN3456_CHICHI.06_TCU049N
Landers	1992	7.28	48.84	292.12	RSN3754_LANDERS_INJ180
Parkfield	2004	6.00	0.80	307.59	RSN4117_PARK2004_Z15090
Chuetsu	2007	6.80	28.97	334.01	RSN4840_CHUETSU_65003EW
Chuetsu	2007	6.80	21.40	245.45	RSN4855_CHUETSU_65024EW
Christchurch	2011	6.20	5.58	207.00	RSN8130_CCHURCH_SHLCS50E
San Simeon	2003	6.52	37.92	1100.00	RSN8167_SANSIMEO_DCPP247

In another shake-table experiment [18,19], the authors were also able to tighten the braces by hand and noted that this was sufficient to stiffen the frame. In doing so, they reduced the fundamental period from 0.8 sec (with slackness) to the expected period of 0.4 sec (no slackness). Aside from this, the effect on the overall system performance was negligible. When the frame sways in one direction, the brace within the shortening diagonal loses pre-tensioning and becomes slack temporarily. This provides sole control of the system's performance to the brace in the lengthening diagonal. Tension in both braces is only present when the structure returns to the upright position. Therefore, the pre-tensioning only causes the frame to stiffen at the upright position and does not affect the behaviour during the deformed position.

NONLINEAR TIME-HISTORY ANALYSES

Nonlinear time-history analyses were performed to assess the automated tuning procedure and examine whether the structure will respond with the deformation profile intended. A set of 30 ground motions were obtained from the PEER NGA-West2 database. They were chosen based on the goodness-of-fit of their scaled spectra with the target (design) spectrum over a range of periods from 0.1–2 sec, which accounts for higher mode and period-lengthening effects.

The selection process includes an imposed criteria of the maximum acceleration being no more than 1.5 times the target acceleration throughout the spectrum. Figure 8 shows the target spectrum and average spectrum of the ground motions. Table 4 lists the ground motions selected.

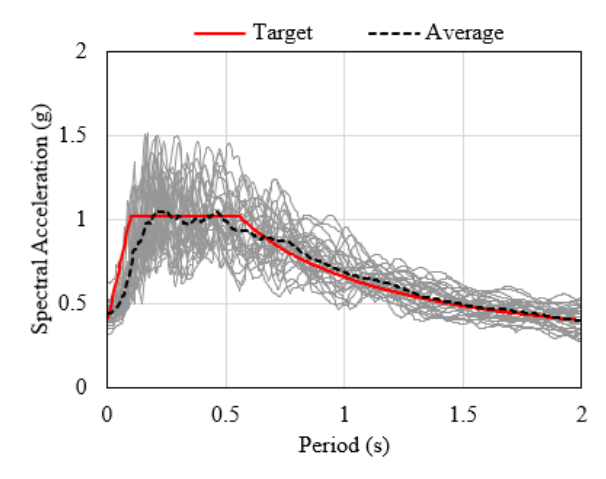


Figure 8: Acceleration spectra of the ground motions.

Time-history analyses were performed using Newmark's direct integration method with constant (average) acceleration over each time-step. A time-step of 0.002 sec was used for all analyses.

As the modelled structure had modal periods of 0.1 sec (higher mode), 0.4 sec (fundamental mode), and 0.9 sec (effective period), Rayleigh damping ratios of 1.5% were set at the periods of 0.1 and 0.9 sec with the curve reaching a minimum of 0.9% at 0.3 sec.

Figures 9 and 10 show the results in terms of the peak response values from each ground motion. On average, the peak base shear is 4870 kN, which slightly exceeds the design value of 4449 kN by 10%. As Table 5 shows, the peak floor displacements also exceed the target/design values by 15%, 9% and 3% for the first, second and third floors respectively.

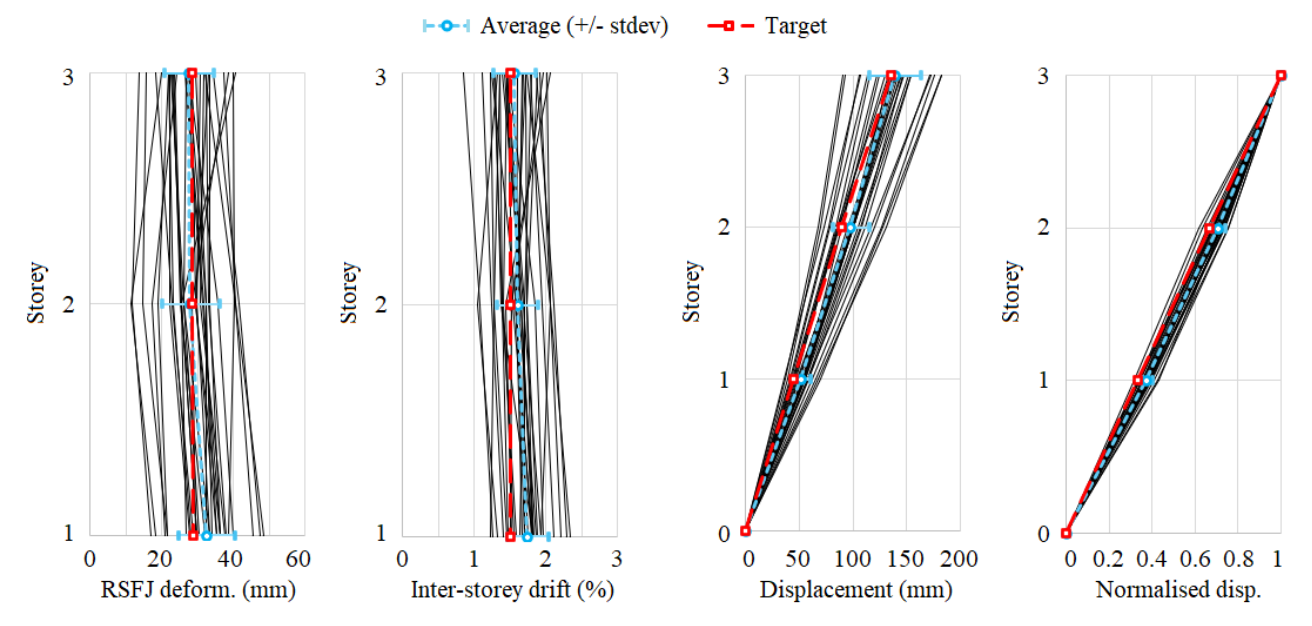


Figure 9: Peak (a) RSFJ deformations, (b) inter-storey drifts, (c) floor and (d) normalized floor displacements.

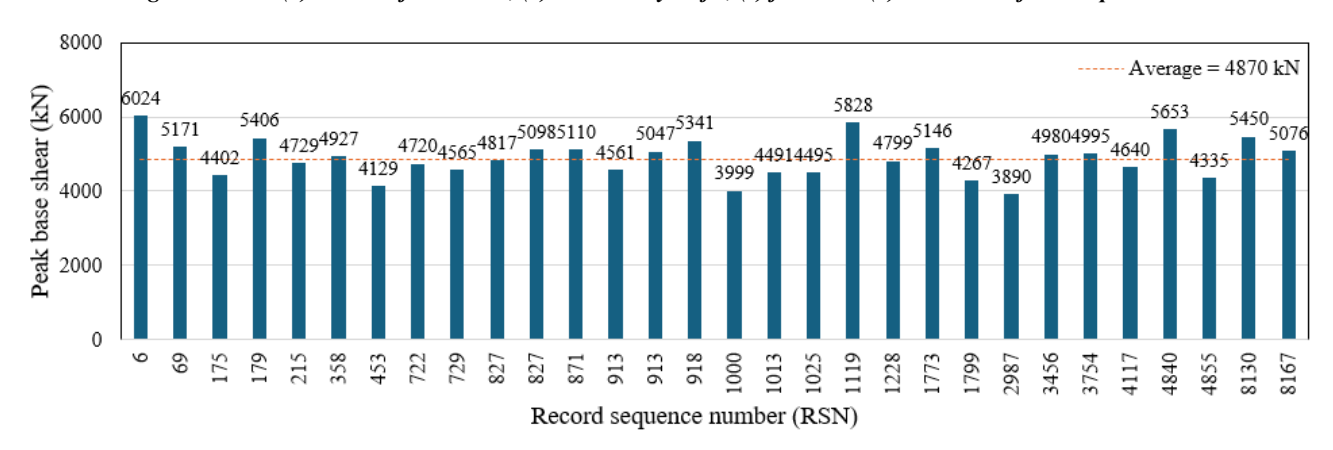


Figure 10: Peak base shear in response to each ground motion.

Table 5: Comparing target and response variables from the time-history analyses.

Storey num.	Storey displacement, U_i (mm)			Normalized storey disp., U_i/U_3			Inter-storey drift (%)			RSFJ deformation, Ursfj (mm)		
i	Target	Average	Error	Target	Average	Error	Target	Average	Error	Target	Average	Error
3	135	139.0	3%	1	1	-	1.50	1.56	4%	28.4	27.6	3%
2	90	97.7	9%	0.67	0.70	4%	1.50	1.60	7%	28.4	27.9	2%
1	45	51.6	15%	0.33	0.37	12%	1.50	1.74	16%	28.7	32.4	13%

The displacement envelope is larger at the lower floors, along with the inter-storey drift and RSFJ deformation. This is typical for braced frames and largely influenced by the load pattern selected when tuning the dampers. However, when the individual displacements are normalised by the top floor displacement, the resulting envelopes are approximately linear. The results show that the proposed procedure can be used to tune the dampers effectively to achieve the desired linear shape and a satisfactory match with the roof displacements required.

CONCLUSIONS

The RSFJ is a versatile damper characterised by highly customisable load-deformation behaviour. To take advantage of this, however, requires a certain degree of experience and intuition in seeking the combination of damper parameters needed to produce a desired hysteresis. This paper presents a systematic and objective procedure to determine damper parameters from a flag-shape specified by the user.

The derived equations were validated with existing experimental data. Building on this, the procedure was extended to demonstrate how to tune the RSFJ dampers simultaneously to achieve a structural response desired by the user. A three-storey building was designed, tuned and analysed through nonlinear time-history analyses with a set of 30 ground motions from the PEER NGA-West2 database.

The average roof displacement was very close to the design displacement (3% error) with larger errors towards the bottom floor (9% for 2nd floor, 15% for 1st floor). When normalised by the top floor displacements, the resulting envelopes show an approximately linear shape.

Peak RSFJ deformations were also close to the design values, only exceeding them by 3%, 2% and 13% at the top, 2nd and 1st floors respectively. On average, the base shear of 4870 kN exceeded the design value of 4449 kN by about 10%.

The results show that the proposed procedure is effective at tuning the dampers to achieve a uniform deformation profile and the displacement amplitudes intended from a displacement-based design. Avenues for future studies include examining other structural systems and placement of dampers.

ACKNOWLEDGEMENTS

The constructive and detailed feedback from the reviewers have been invaluable for improving the manuscript; their contributions are acknowledged with gratitude.

REFERENCES

- Abeling S, Ferner H, Hugh C, Gill D, Brown C, Beaven S, Brunsdon D, Dunne C, Elwood K, Hare J and Jury R (2024). "The Resilient Buildings Project. Relating Societal Expectations to Building Seismic Performance: Report for Stage 3". New Zealand Society for Earthquake Engineering Annual Conference, Wellington, 59pp. https://www.nzsee.org.nz/db/PUBS/RBP_Stage_3_Final-Report_Rev2_Feb2024.pdf
- 2 Davis M and Porter K (2016). "The public's role in seismic design provisions". *Earthquake Spectra*, 32(3): 1345-1361. https://doi.org/10.1193/081715EQS127M
- 3 Fang C, Qiu C, Wang W and Alam MS (2023). "Self-centering structures against earthquakes: a critical review". *Journal of Earthquake Engineering*, **27**(15): 4354–4389. https://doi.org/10.1080/13632469.2023.2166163

- 4 Zarnani P, Valadbeigi A and Quenneville P (2016). "Resilient Slip Friction (RSF) joint: A novel connection system for seismic damage avoidance design of timber structures". 10th World Conference on Timber Engineering, August 22-25, Vienna, Austria, 9pp. http://hdl.handle.net/20.500.12708/172
- 5 Chan N, Hashemi A, Zarnani P and Quenneville P (2023). "Pinching-free connector in a self-centering braced frame". *Journal of Structural Engineering*, 149(7): 04023083. https://doi.org/10.1061/JSENDH.STENG-12211
- 6 Chan N, Hashemi A, Zarnani P and Quenneville P (2019). "Pinching-free connector for seismically resistant timber structures: experimental validation and numerical simulation". 2019 Pacific Conference on Earthquake Engineering, April 4-6, Auckland, New Zealand, 10pp. https://db.nzsee.org.nz/2019/Oral/4B.12%20Chan.pdf
- 7 Yousef-beik SMM, Veismoradi S, Zarnani P and Quenneville P (2024). "Design and testing of a self-centering friction damper-brace for compression ultimate limit state: inelastic buckling". *Structures*, **62**: 106166. https://doi.org/10.1016/j.istruc.2024.106166
- 8 Wang Y, Zhou Z, Zhang L and Zhao K (2023). "Hysteretic behavior of dual-self-centering variable friction damper braces with low pretensioned force". *Journal of Earthquake Engineering*, 27(1): 142-161. https://doi.org/10.1080/13632469.2021.1997840
- 9 Zhang P, Yam MCH, Ke K, Song Y and Zhu M (2024). "Experimental study of a self-centering damper with multistage energy-dissipation mechanism". *Journal of Structural Engineering*, 150(11): 04024166. https://doi.org/10.1061/jsendh.steng-13665
- 10 Chan N, Hashemi A, Zarnani P and Quenneville P (2021). "Damping-ductility relationships for flag-shaped hysteresis". *Journal of Structural Engineering*, 147(7): 04021093. https://doi.org/10.1061/(asce)st.1943-541x.0003055
- 11 Christopoulos C, Filiatrault A and Folz B (2002). "Seismic response of self-centring hysteretic SDOF systems". *Earthquake Engineering and Structural Dynamics*, 31: 1131–1150. https://doi.org/10.1002/eqe.152
- 12 Bagheri H, Hashemi A, Yousef-beik SMM, Zarnani P and Quenneville P (2020). "New self-centering tension-only brace using resilient slip-friction joint: experimental tests and numerical analysis". *Journal of Structural Engineering*, **146**(10): 04020219. https://doi.org/10.1061/(asce)st.1943-541x.0002789
- 13 Darani FM, Zarnani P, Veismoradi S, Yousef-beik SMM, Hashemi A and Quenneville P (2021). "Resilient slip friction joint performance: component analysis, spring model and anti-locking mechanism". *Structures*, **33**: 3897–3911. https://doi.org/10.1016/j.istruc.2021.06.075
- 14 Hashemi A, Zarnani P, Masoudnia R and Quenneville P (2017). "Seismic resistant rocking coupled walls with innovative Resilient Slip Friction (RSF) joints". *Journal of Constructional Steel Research*, 129: 215–226. https://doi.org/10.1016/j.jcsr.2016.11.016
- 15 Priestley MJN, Calvi GM and Kowalsky MJ (2007). "Displacement-Based Seismic Design of Structures". ISBN: 978-88-6198-0006. IUSS Press, Pavia, Italy. 721pp.
- 16 Dhakal RP, Pourali A, Tasligedik AS, Yeow T, Baird A, Macrae G, Pampanin S and Palermo S (2016). "Seismic performance of non-structural components and contents in buildings: an overview of NZ research". Earthquake Engineering and Engineering Vibration, 15: 1–17. https://doi.org/10.1007/s11803-016-0301-9

- 17 Bommer JJ and Mendis R (2005). "Scaling of spectral displacement ordinates with damping ratios". *Earthquake Engineering and Structural Dynamics*, **34**(2): 145–165. https://doi.org/10.1002/eqe.414
- 18 Assadi S, Hashemi A, Clifton C, Quenneville P, MacRae G, Bagheri H, Jia L-J, Yan Z and Zarnani P (2024). "Shaketable testing of the resilient slip friction joints". New Zealand Society for Earthquake Engineering Annual Conference, April 9-11, Wellington, New Zealand, 14pp. https://repo.nzsee.org.nz/handle/nzsee/2677
- 19 Chan N, Hashemi A, Assadi S, Clifton C, MacRae G, Dhakal R, Jia L-J and Quenneville P (2025). "Shake-table tests of a three-storey steel structure with resilient slip-friction joints (RSFJ)". *Journal of Structural Engineering*, (Under review).

https://doi.org/10.48550/arXiv.2509.03452